Annual Status Report-August 1995
Cooperative Agreement No. NCC1 - 169

Name and address of Institution:
North Carolina State University
Mechanical & Aerospace Engineering Department
Raleigh NC 27695-7910
(919) 515 - 5667

Title: **Semi-Span Model Testing in the National Transonic Facility**

Principal Investigator:
Dr. Ndaona Chokani
Research Assistant:
William E. Milholen II

NASA Technical Officer:
L. Elwood Putnam
NASA Langley Research Center
Facilities Research Branch
AAD MS 267
(804) 864 - 5116

Introduction

Over the past several years, transport designers have expressed a renewed interest in semi-span model testing, particularly for the design of advanced subsonic transport aircraft[1]. Historically, transport aircraft have been designed in ground test facilities at Reynolds numbers significantly lower than flight conditions. However, a configuration optimized in a ground test facility at reduced Reynolds numbers may perform differently at flight conditions. The extrapolation of low Reynolds number data to flight conditions became even more problematic as wing design methods began to mature. Since modern wing designs are generally optimized for a given cruise condition, their off-design performance is often poor[2]. This behavior significantly increases the risk of relying on low Reynolds number data. Thus, it is necessary to design and test advanced subsonic transport configurations at flight Reynolds numbers.

Only the NASA Langley Research Center's National Transonic Facility (NTF) presently has the potential to provide the capability of testing advanced configurations at full-scale Reynolds numbers. However, a conventional full-span model is not well suited for the testing of advanced configurations due to the relatively small size of the control surfaces. The difficulty in accurately positioning these components can result in poor repeatability of the test data. In addition, aeroelastic deformations may introduce significant errors into the test data. Thus, a semi-span model test technique has been proposed for the NTF. Figure 1 shows a comparison between a conventional full-span model, mounted in the center of the test section, and a semi-span model mounted on the test-section sidewall. The primary advantage of semi-span model testing is the increased Reynolds number capability due to the

larger model size. The increased model size also allows for more accurate positioning of the model components, improved model fidelity, and increased model stiffness; all these features improve the data quality[2,3]. In spite of these advantages, the use of a semi-span model introduces additional difficulties which must be addressed in the semi-span test procedure. These difficulties include the effects of increased wind-tunnel wall interference due to the increased model size[4], and the effects of the semi-span model mounting. The latter is the concern of the present research. The presence of the boundary layer on the wind-tunnel sidewall results in the loss of symmetry about the model centerplane. Previous research[5] has shown that the sidewall boundary layer may adversely affect the flow over a semi-span model. An improved understanding of the influence of the sidewall boundary layer is a key to the successful implementation of the semi-span model test technique in the NTF.

The objectives of the present research are: (a) to develop a computational approach to support semi-span model test techniques in the NTF; and (b) to integrate this approach with the conduct of an experimental test program. To meet these objectives, the following approach is taken. A state-of-the-art three-dimensional Navier-Stokes solver is employed to compute the flow over both a full-span configuration and a semi-span configuration mounted on the sidewall of the tunnel. The computations are validated by making direct comparisons to experimental data for both configurations. Then, the semi-span computational results are compared to the full-span results to document how the flow over the semi-span configuration differs from that over the full-span configuration. The results of this comparative study will be used to provide a conceptual framework within which a semi-span model test technique may be implemented in the NTF.

Experimental background

The full-span Energy Efficient Transport (EET) model described in Reference 6 was tested extensively in the NASA Ames Research Center's 12-Foot Pressure Tunnel. The aspect ratio of the wing was 10.0, with a quarter-chord sweep angle of 27° and a dihedral angle of 5°. The wing was constructed of supercritical airfoil sections, with a nonlinear twist distribution. In the experiment, force and moment data were acquired along with wing pressure data at three spanwise locations.

After the full-span configuration testing, the full-span model was modified to become the NTF semi-span model[7]. Figure 2 shows a schematic diagram of the semi-span configuration which is examined in the present investigation. A non-metric stand-off geometry was used to support the model away from the wind-tunnel sidewall. The profile shape of the stand-off was identical to that of the full-span fuselage symmetry plane. Surface pressure data on the stand-off and fuselage were obtained in the experiment to document the flow in the near-wall region. In addition, surface pressure data at two spanwise locations on the wing, and force and moment data were also obtained.

Numerical Procedure

Computational code

The low speed flow over the full-span and semi-span cruise configurations were examined using the computational code TLNS3D-MB[8] which was developed at the NASA Langley Research Center. The code solves the time-dependent, three-dimensional, thin-layer compressible Navier-Stokes equations on block-structured, body-fitted grids. The governing equations are discretized in a central difference, finite volume formulation. An explicit second-order accurate Runge-Kutta time-stepping scheme is used to numerically integrate the equations. Since the solutions of interest are steady state, the code takes advantage of several acceleration techniques including multigrid, grid sequencing, and local time stepping. In the first phase of the present investigation, the performance of TLNS3D-MB at the low freestream Mach numbers was evaluated[9]. The results of the evaluation indicated that TLNS3D-MB was capable of accurately and efficiently computing flows around complex three-dimensional configurations at low freestream Mach numbers.

Boundary conditions

The boundary conditions used for the full-span and semi-span computations are as follows. The far-field outer boundary is treated using characteristic boundary conditions. The properties at the downstream boundary are obtained using a zeroth-order extrapolation from the interior. The fuselage and wing surfaces are treated as adiabatic, no-slip surfaces, with the normal pressure gradient set to zero at the surface. For the semi-span configuration, the stand-off surface is also treated as a no-slip surface. It should however be noted that this surface is *not* included in the force and moment calculations since the stand-off is non-metric in the experiment. The final boundary condition is the root plane. For the full-span computations, symmetry conditions are used, resulting in a "free-air" simulation. For the semi-span computations, the root plane is treated as a no-slip surface in order to simulate the wind-tunnel sidewall boundary layer.

Grid generation

Figure 3 shows partial views of the C-O grid topologies used for both the full-span and semi-span computations. The multiblock structured grids were generated using GRIDGEN[10]. Grid points are clustered in the streamwise, normal, and spanwise directions to resolve the expected large flow gradients. The far-field boundaries are located six semi-span lengths from the model, which corresponds to approximately 18 root chord lengths. The grid for the full-span model is comprised of 2 blocks, while the semi-span grid has 6 blocks.

Results and Discussions

Full-span computations

Initially, computations were carried out with four grids simulating fully turbulent flow using the Baldwin-Lomax turbulence model. Figure 4 shows a comparison of the computational results with experimental data for $M_\infty = .20$, $\alpha = 4.43°$, and $Re = 4.2 \times 10^6$. The grid dimensions, such as $241 \times 65 \times 81$, represent the number of grid points in the streamwise, normal, and spanwise directions respectively. It is seen that refinement of the grid improves the agreement with experimental data, particularly in the leading edge region. Further streamwise refinement up to 481 points was examined; the results obtained were identical within plotting accuracy to those obtained with the $241 \times 65 \times 81$ grid. Thus the $241 \times 65 \times 81$ grid was used in the following computations. For this grid, the wing surface grid dimensions were 145×61. The typical values of y^+ for the first grid point off the wing surface *and* fuselage were in the range of 1-5, with approximately 25 grid points clustered in the boundary layer.

The computed pressure distributions with the zero-equation Baldwin-Lomax and one-equation Spalart-Allmaras turbulence models are plotted in Figure 5. It can be seen that the computations using the one-equation model are in better agreement with the experimental data. At all three stations, the suction peak level is more accurately predicted, as is the subsequent adverse pressure gradient. It is also evident that the pressure distribution over the *whole* wing is influenced by the turbulence model. Two higher angles of attack (8.58° and 12.55°) were also investigated, and also confirmed that the one-equation model consistently gave better predictions. The one-equation turbulence model of Spalart-Allmaras was thus used in the following computations.

Figure 6 shows a comparison of the computed lift and pitching moment coefficients with experimental data. The computations were performed at $\alpha = 4.43°$, 8.58°, and 12.55°. Overall, the agreement between the experiment and computations is quite good. Figure 7 shows the pressure distributions at $\alpha = 8.58°$. Across the span of the wing, the computed pressure distributions are in excellent agreement with the experimental data. The leading edge suction peaks and their associated strong adverse pressure gradients are well resolved. Similar agreement was obtained at the highest angle-of-attack. Given such agreement, the Navier-Stokes solver was then used to compute the flow over the semi-span configuration.

Semi-span computations

A fully turbulent boundary layer representative of that measured in a recent NTF experiment[11] was modeled along the sidewall of the semi-span configuration. The results of a grid refinement study showed that 33 points clustered in the sidewall boundary layer were adequate to resolve the details of the flow in the near wall region. Figure 8 presents a comparison of computed lift and pitching moment coefficients with *uncorrected* data from the NTF tests. The computations were performed at the same angles-of-attack as discussed above. It should be noted that consistent with the experimental method, the force and moment coefficients are computed *only* on the wing and fuselage. Again the computations agree quite well with the experimental data.

Figure 9 shows the comparison of the computed pressure distributions with *uncorrected* experimental data at two spanwise locations on the wing for the case $\alpha = 8.24°$. The computations show good qualitative agreement with the experimental data. Across the span, the leading edge suction peaks and strong adverse pressure gradients are well predicted. The mismatch in pressures suggests that the computational and experimental angles-of-attack differ. It should be noted that the experimental data has not been corrected for the effects of the wind-tunnel wall interference, which may account for the apparent difference in angle-of-attack. To further demonstrate the capabilities of the Navier-Stokes solver, a comparison of the predicted pressure distribution at the midspan section of the stand-off geometry and *uncorrected* experimental data is shown in Figure 10. For reference, the location of the wing root is shown. Again, the qualitative agreement between the pressure distributions is quite good. The multiple adverse pressure gradients along the stand-off have been adequately predicted. Since the stand-off is immersed in the sidewall boundary layer, this comparison indicates that the Navier-Stokes solver is capable of predicting the near-wall behavior resulting from the interaction of the sidewall boundary layer and the flow over the semi-span model. In the following section the semi-span computational results are compared with the full-span results, to determine in detail how the flows over the semi-span and full-span configurations differ.

Comparison of full-span and semi-span configuration flow fields

Figure 11 shows a comparison of the computed and experimental lift and pitching moment coefficients for *both* configurations. The full-span and semi-span results differ in several aspects. Firstly, the lift coefficients are higher for the semi-span configuration. Secondly, the lift curve slope for the semi-span configuration is greater than that of the full-span. And finally, the semi-span pitching moment curve has been shifted upward. These observations suggest that the stand-off distance from the sidewall is too large[1]. Although the computed values are slightly off-set from the experimental data, the computations correctly predict the incremental shifts observed in the data. Since the semi-span configuration generates more lift for a given angle-of-attack, one may conclude that the semi-span model is at an effective higher angle-of-attack. An examination of the computed pressure distributions, however shows that this is incorrect. In general, when the angle-of-attack is increased, the pressure distribution on *both* the upper and lower wing surface changes. The C_p values on the upper surface become more negative, while the C_p values on the lower surface become more positive. The computed pressure distributions for both configurations at $\alpha = 4.43°$ are plotted in Figure 12. It is observed that the pressure distribution on the lower surface of the wing is *not* significantly altered. In contrast, the upper surface pressure distribution for the semi-span model has been altered. The flow over the upper surface of the semi-span wing is more accelerated, thus decreasing the pressure. It is also important to note that the flow acceleration on the upper wing surface is not limited to the leading edge region, but extends up to the trailing edge at all 3 stations. The net result of this flow acceleration is that the lift on the semi-span configuration is increased. The same effect of the flow acceleration is seen in Figure 13, where the $\alpha = 8.58°$ case is shown. This effect is more clearly illustrated in Figure 14, where the difference between the full-span and semi-span pressure coefficients is plotted. As the angle-of-attack is increased, the maximum difference between the full-span and semi-span upper surface pressure coefficients is also increased. At

the highest angle-of-attack, $\alpha = 12.55°$, the maximum difference is found to be on the order of unity.

Figure 15 shows a comparison of the predicted spanwise load distributions for both configurations at all three angles-of-attack. The wing-fuselage juncture occurs at $\eta = .1095$. This comparison graphically demonstrates how the flow acceleration over the upper wing surface of the semi-span configuration results in an increased wing loading across the entire span. Clearly, the influence of the stand-off geometry and sidewall boundary layer is not limited to the inboard portion of the wing. Further flow field comparisons also show that the flow acceleration over the semi-span model is not limited to the wing alone.

The predicted pressure distributions along the centerline of the fuselage at $\alpha = 12.55°$ are compared in Figure 16. The semi-span configuration experiences a significant flow acceleration over the upper surface of the fuselage. As with the wing, the flow acceleration is not limited to the nose region alone, but extends downstream to the wing-fuselage juncture region. In contrast to the wing, the lower surface pressure distribution along the fuselage of the semi-span configuration is altered noticeably. The flow along the lower fuselage surface has been accelerated as compared to the full-span configuration. Further examination of the semi-span computational results shows that the stand-off geometry behaves as a lifting surface. Even though the lift generated by the stand-off geometry is *not* included in the force and moment calculations, the circulation of the entire flow is increased. As a result, a flow acceleration is induced over the upper surface of the semi-span configuration. Decreasing the stand-off distance from the sidewall may be expected to minimize the induced acceleration.

The upper wing surface streamline patterns are shown in Figure 17 to examine in further detail how the semi-span flow field differs from that of the full-span. Here the $\alpha = 12.55°$ case is used as the illustrative example. Both solutions predict flow separation along the trailing edge of the wing. The location and extent of the separation is quite similar for both configurations. On the inboard portion of the wing, the streamline patterns differ significantly. The semi-span configuration shows a larger crossflow, particularly near the trailing edge. It is anticipated that the increased crossflow on the inboard portion of the semi-span wing may adversely affect the stall characteristics. This may account for the tendency of a semi-span model to stall inboard[1].

Figure 18 shows a comparison of the predicted streamline patterns at the root plane for each configuration at $\alpha = 12.55°$. For the full-span configuration this is the centerline of the fuselage, while for the semi-span configuration, this is the simulated wind tunnel sidewall. The full-span solution predicts smooth flow over the fuselage, exhibiting little streamline curvature. In sharp contrast, the semi-span computation predicts that the sidewall boundary layer separates upstream of the stand-off, and rolls up to form a horseshoe vortex in the juncture region. As a result, significant streamline curvature occurs. Figure 19 shows details of the predicted flow patterns on the sidewall in the nose region of the stand-off. The saddle point and dividing streamlines of the separation are clearly visible, along with the subsequent flow reversal near the nose of the stand-off. Similar results were obtained at the other angles-of-attack. This again demonstrates that the flow over the semi-span model differs markedly from the flow over the full-span configuration.

Finally, Figure 20 presents a comparison of computed sidewall streamline patterns and

experimental tuft visualization results for $\alpha = 8.24°$. The agreement is excellent. The location of the saddle point and subsequent flow reversal in the nose region are well predicted by the computation. This comparison further demonstrates the capabilities of the Navier-Stokes solver to aid in the development of a semi-span model test techniques in the NTF. It should be noted that the computational results were used to determine the location of tufts on the wind-tunnel sidewall. This is just one example of how computational results may be successfully integrated with an experimental test program.

Conclusions

A computational investigation was performed to support the development of a semi-span model test capability in the NASA Langley Research Center's National Transonic Facility. This capability is required for the design of advanced subsonic transport aircraft. A state-of-the-art three-dimensional Navier-Stokes solver was used to compute the low-speed flow over both a full-span configuration, and a semi-span configuration mounted on the wind-tunnel sidewall. The computational results were validated by making direct comparison to available experimental data for both configurations. The semi-span computational results were compared to the full-span results, to document how the flow over the semi-span configuration differs from that over the full-span.

The aerodynamic characteristics of the semi-span configuration were found to differ markedly from those of the full-span. The semi-span model produced higher lift coefficients, while the pitching moment curve was shifted upward. Comparison of full-span and semi-span surface pressure distributions indicated that the semi-span configuration experienced flow acceleration over its entire upper surface. The flow acceleration increased the wing loading across the entire span. The flow acceleration is believed to be induced by the stand-off mounting geometry. Comparison of predicted upper surface wing streamline patterns further demonstrated the differences between the full-span and semi-span flow fields. On the inboard portion of the wing, the semi-span configuration experienced significantly more cross flow, particularly near the trailing edge. Such behavior is anticipated to adversely affect the stall characteristics.

For all test cases examined, the semi-span computations predicted that the sidewall boundary layer separates upstream of the model, and rolls up to form a horseshoe vortex in the juncture region. The computed sidewall streamline patterns were compared to experimental tuft visualization results, and found to be in excellent agreement. The Navier-Stokes solver will next be used to examine methods to control the sidewall boundary layer, and thus minimize its influence on the flow over the semi-span model.

References

[1] Earnshaw, P.B., Green, A.R., Hardy, B.C. and Jelly, A.H.,"A Study of the Use of Half-Models in High-Lift Wind-Tunnel Testing," AGARD CP515, Oct. 1992, pp. 20.1-20.9.

[2] Goldhammer, M.I. and Steinle Jr., F.W. , "Design and Validation of Advanced Transonic Wings Using CFD and Very High Reynolds Number Wind Tunnel Testing," Proceedings of the 17^{th} International Council of the Aeronautical Sciences, Paper 90-2.6.2, Sept. 1990, pp. 1028-1042.

[3] Boersen, S.J., "Half-Model Testing in NLR High-Speed Wind Tunnel HST, A 1981 Status Report," NLR TR 82123 U, Aug. 1982.

[4] Garriz, J.A., Newman, P.A., Vatsa, V.N., Haigler, K.J. and Burdges, K.P., "Evaluation of Transonic Wall Interference Assessment and Corrections for Semi-Span Wing Data," AIAA Paper 90-1433, June 1990.

[5] Milholen II, W.E. and Chokani, N., "Effect of Sidewall Boundary Layer on Transonic Flow over a Wing," *Journal of Aircraft*, Vol. 31, July 1994, pp. 986-988.

[6] Morgan Jr.,H.L., "Model Geometry Description and Pressure Distribution Data From Tests of EET High-Lift Research Model Equipped with Full-Span and Part-Span Flaps," NASA TM 80048, Feb. 1979.

[7] Johnson, W.G., Jr. , *Private communication*, June 1994.

[8] Vatsa, V.N., Sanetrik, M.D., and Parlette, E.B., "Development of a Flexible and Efficient Multigrid-Based Multiblock Flow Solver," AIAA Paper 93-0677, Jan. 1993.

[9] Milholen, W.E., II and Chokani, N., " A Comparison of Three-Dimensional Compressible Navier-Stokes Codes at Low Mach Numbers", AIAA Paper 95-0767, Jan. 1995.

[10] Steinbrenner, J.P. and Chawner, J.R., "Incorporation of a Hierarchical Grid Component Structure into GRIDGEN," AIAA Paper 93-0429, Jan. 1993.

[11] Adcock, J.B., Private communication, June 1993.

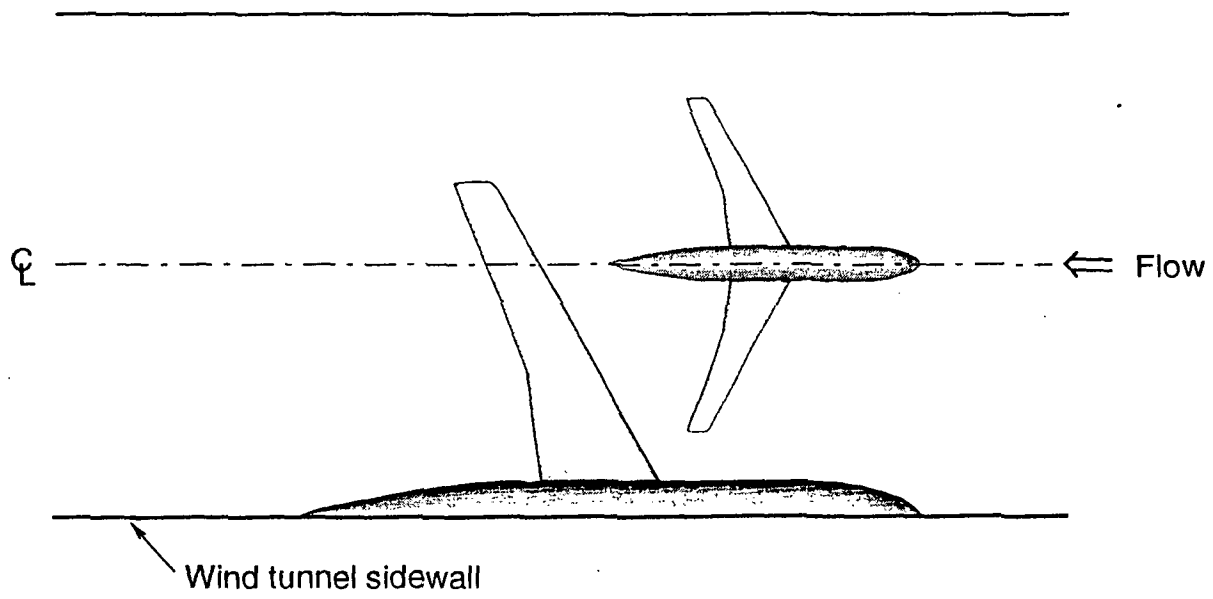

Figure 1: Comparison of semi-span and full-span configurations.

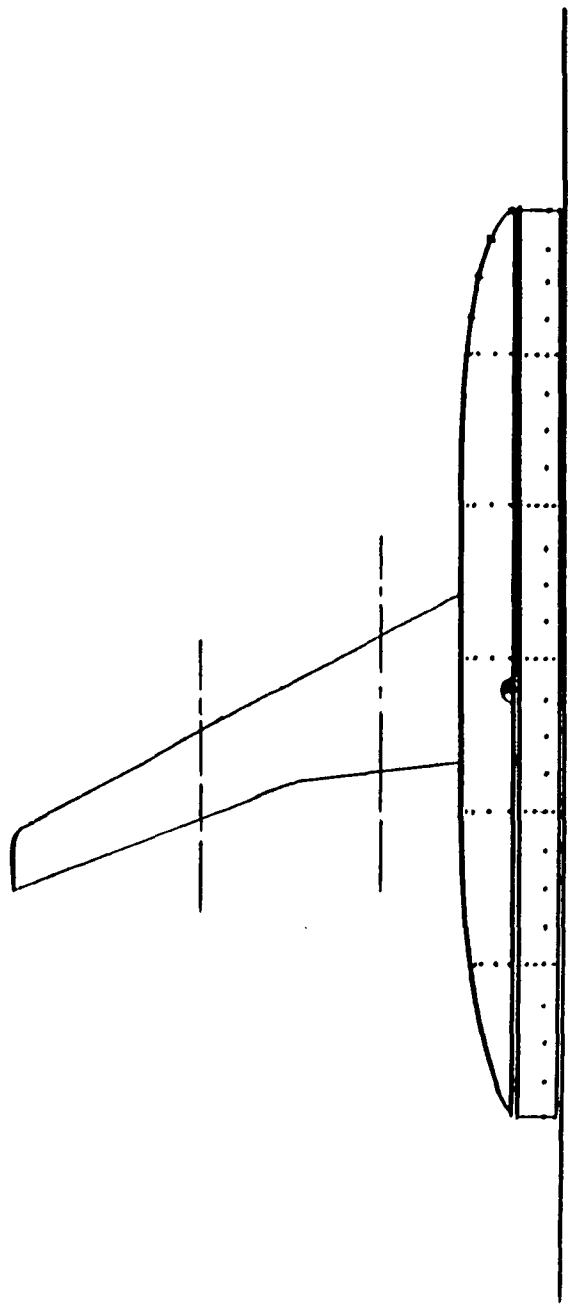

Figure 2: Planform view of semi-span model, with stand-off geometry.

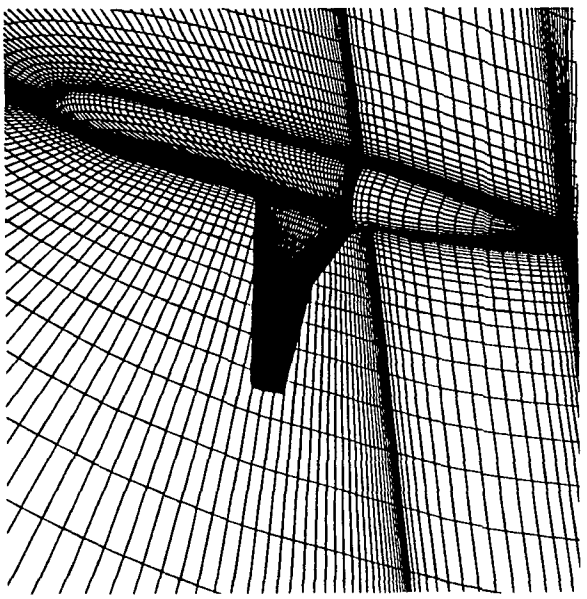

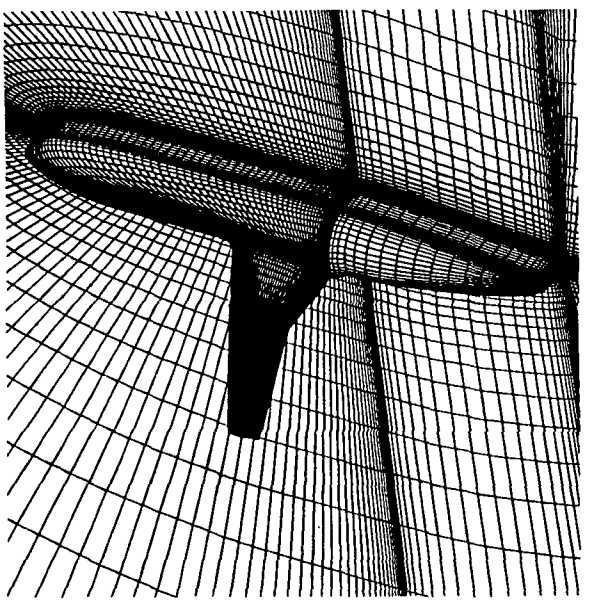

Figure 3: Partial view of C-O grid topologies.

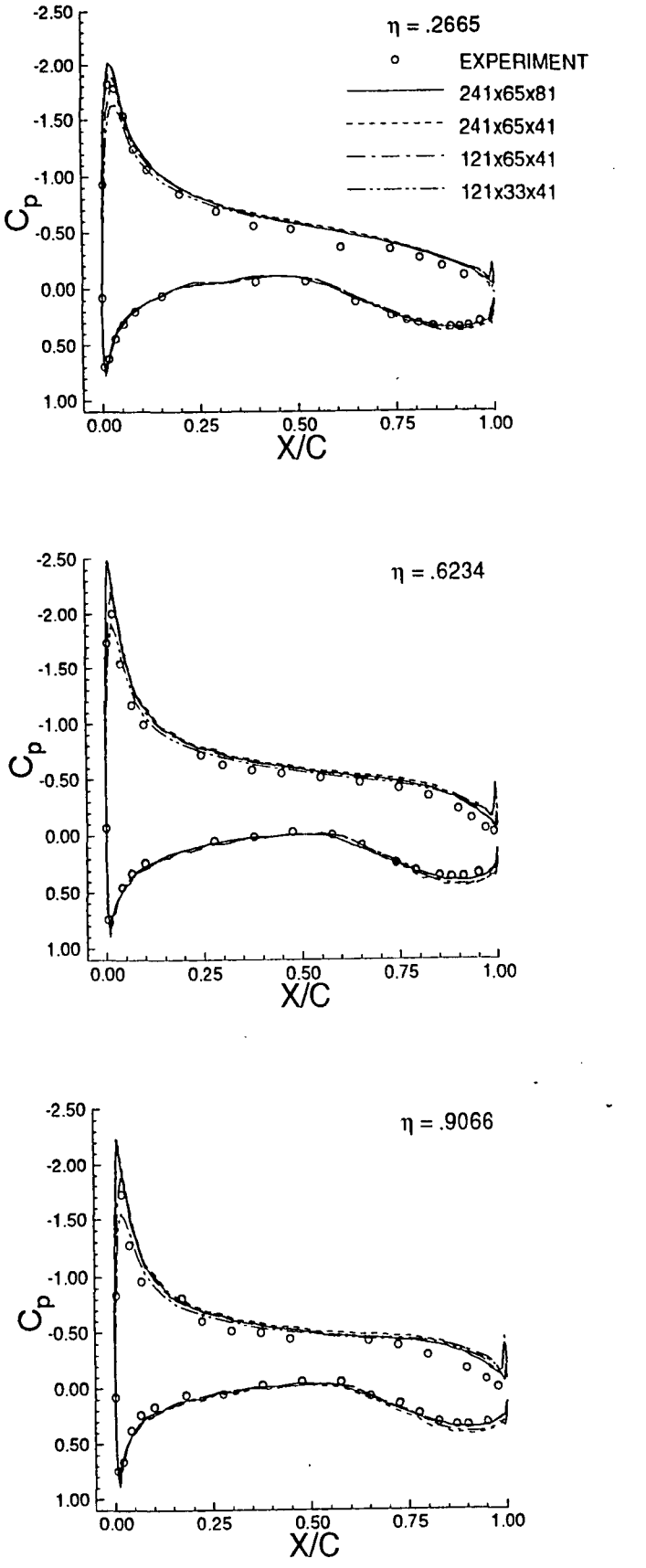

Figure 4: Comparison of computed pressure distributions with experimental data ($M_\infty = .20$, $\alpha = 4.43°$, $Re = 4.2 \times 10^6$).

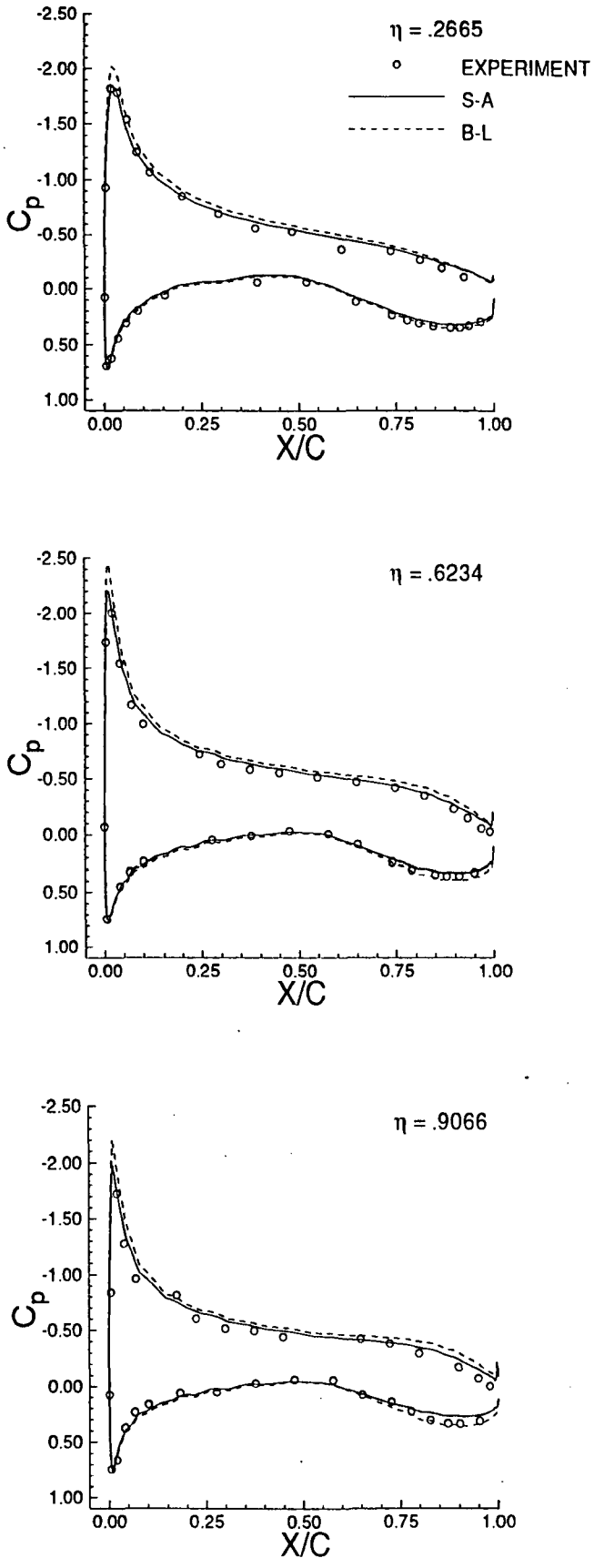

Figure 5: Influence of turbulence model on computed pressure distributions ($M_\infty = .20$, $\alpha = 4.43°$, $Re = 4.2 \times 10^6$).

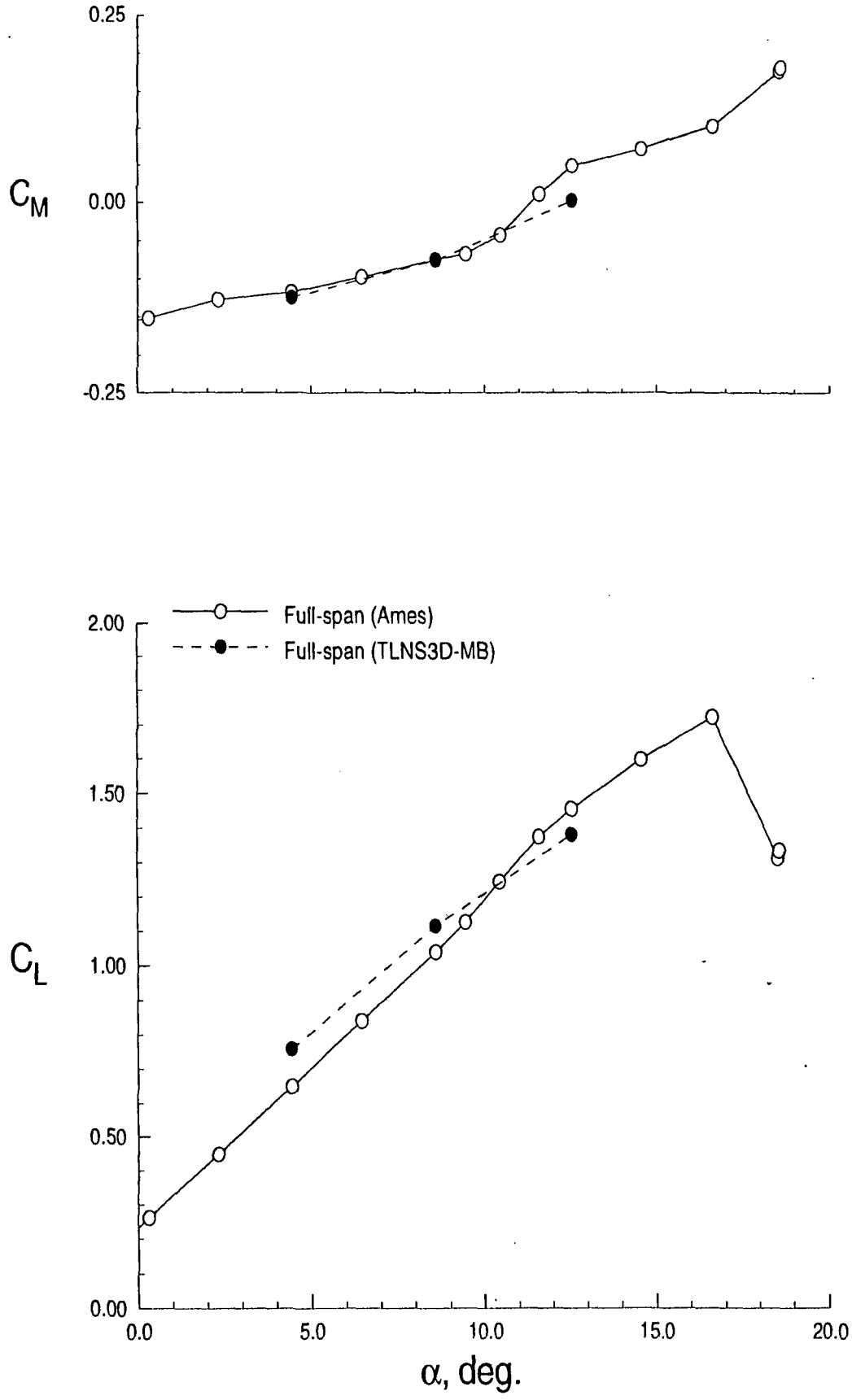

Figure 6: Comparison of computed and experimental full-span lift and pitching moment coefficients ($M_\infty = .20$, $Re = 4.2 \times 10^6$).

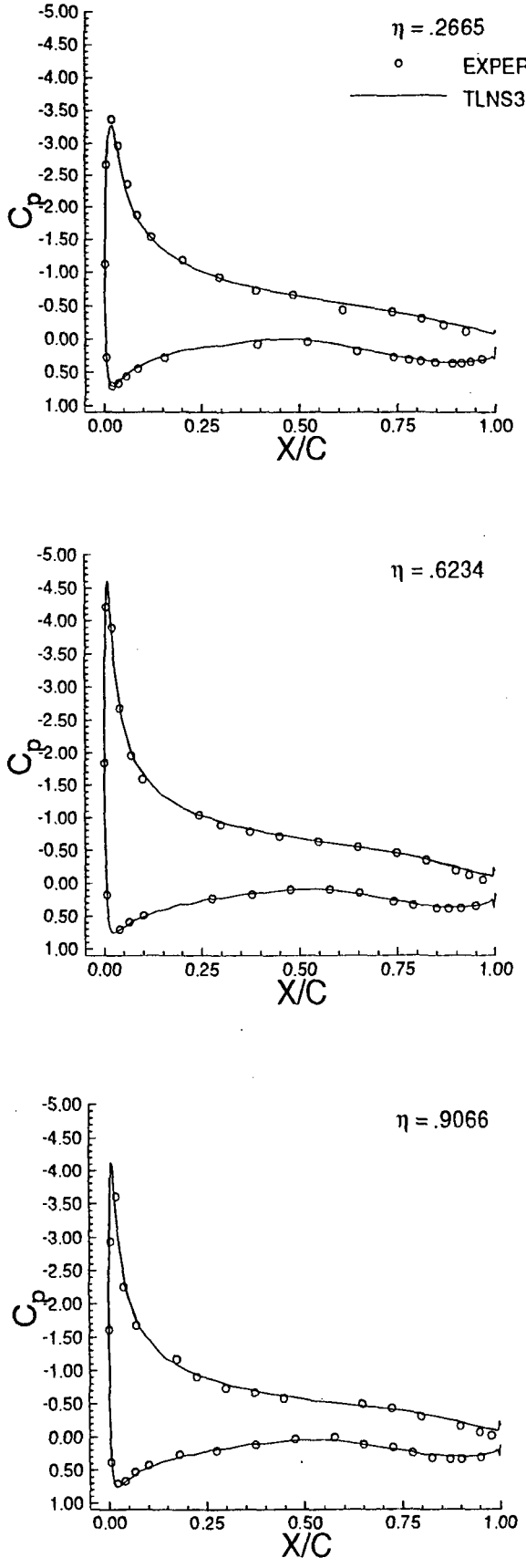

Figure 7: Comparison of computed and experimental full-span pressure distributions ($M_\infty = .20$, $\alpha = 8.58°$, $Re = 4.2 \times 10^6$).

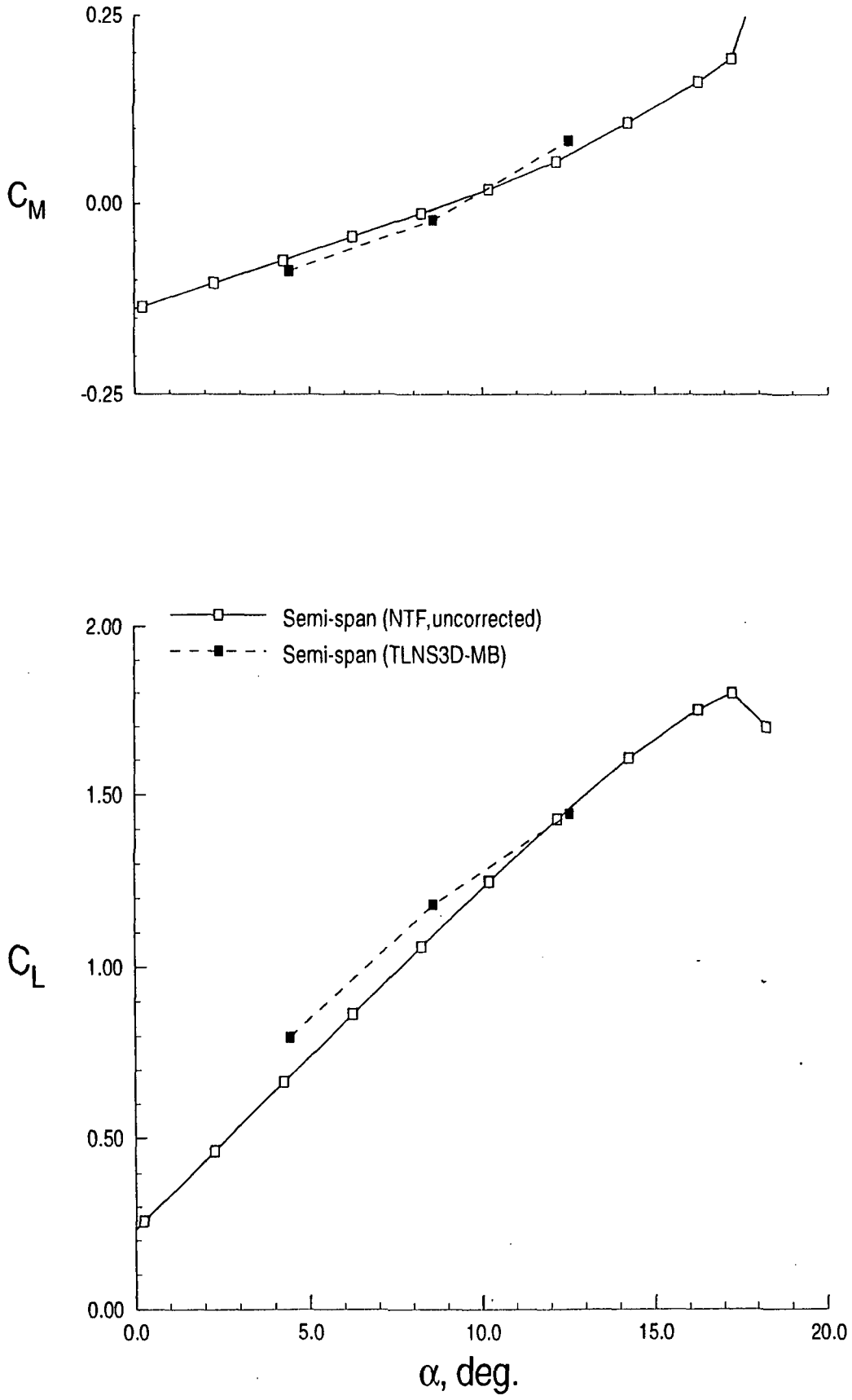

Figure 8: Comparison of computed and experimental semi-span lift and pitching moment coefficients ($M_\infty = .20$, $Re = 4.2 \times 10^6$).

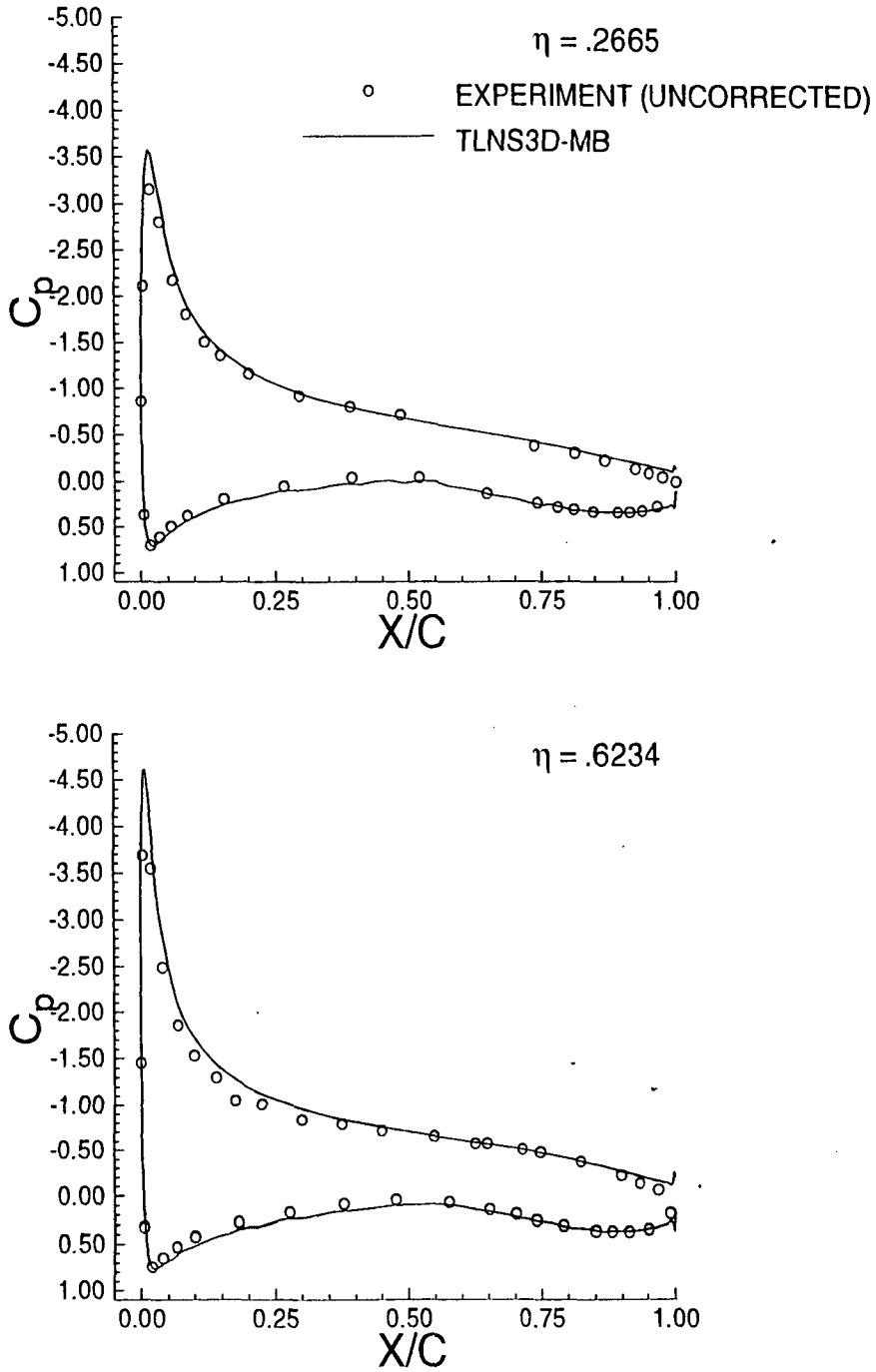

Figure 9:. Comparison of computed and experimental semi-span pressure distributions ($M_\infty = .20$, $\alpha = 8.24°$, $Re = 4.2 \times 10^6$).

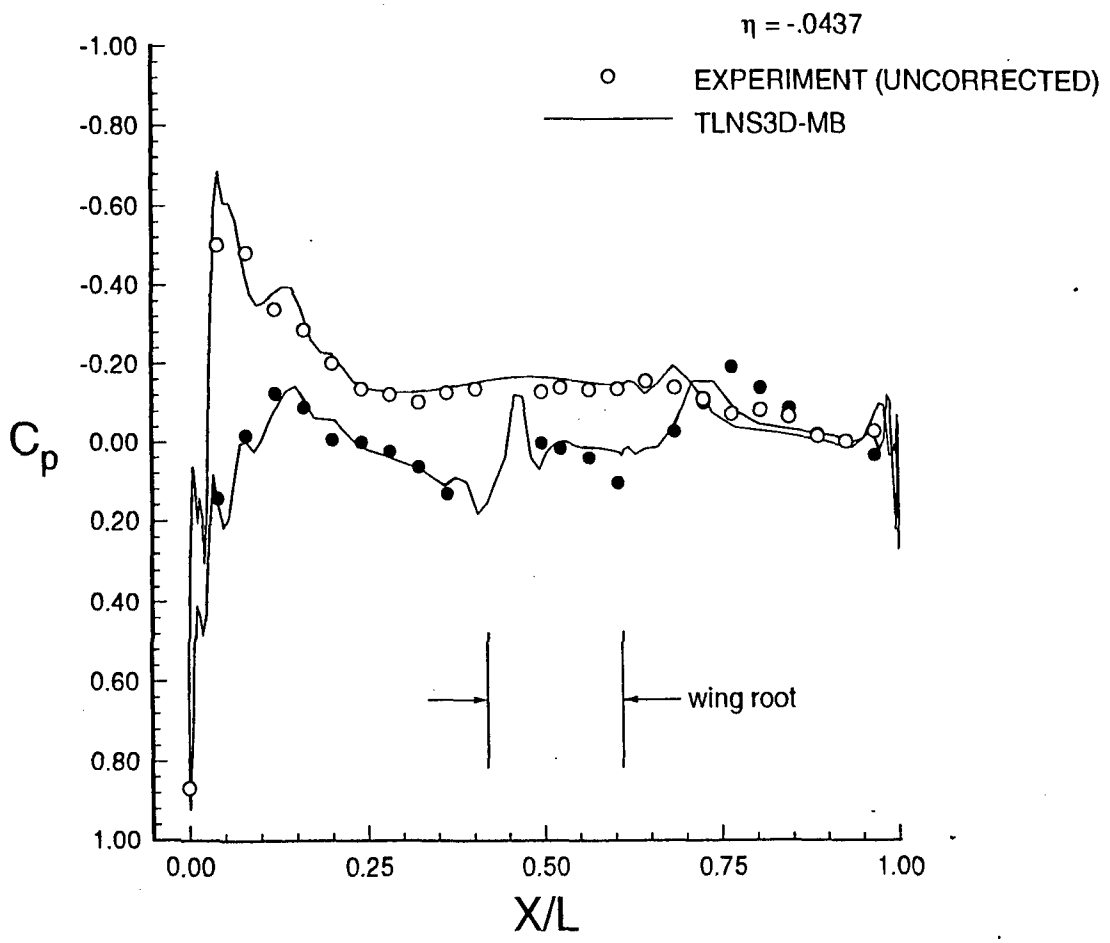

Figure 10: Comparison of computed and experimental semi-span pressure distributions ($M_\infty = .20$, $\alpha = 8.24°$, Re = 4.2 x 10^6).

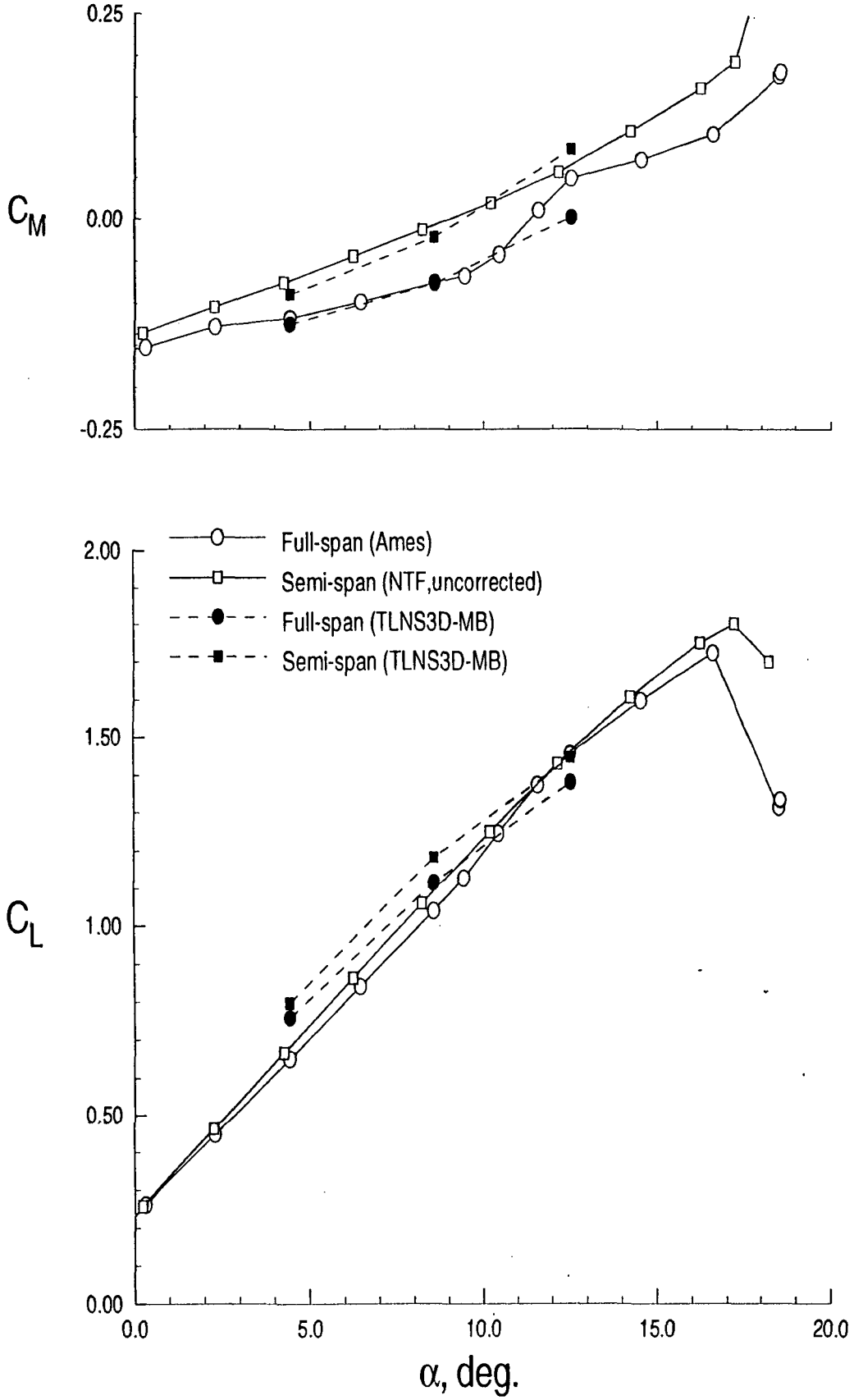

Figure 11: Comparison of full-span and semi-span lift and pitching moment coefficients ($M_\infty = .20$, Re = 4.2 x 10^6).

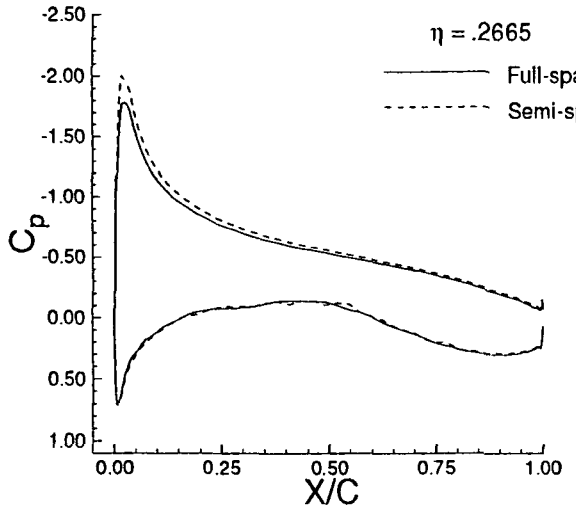

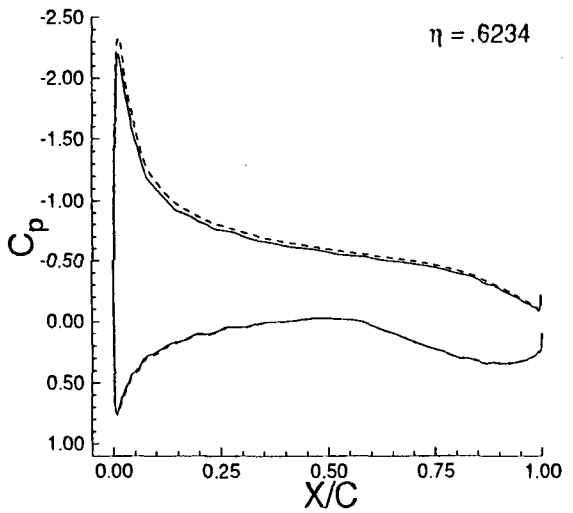

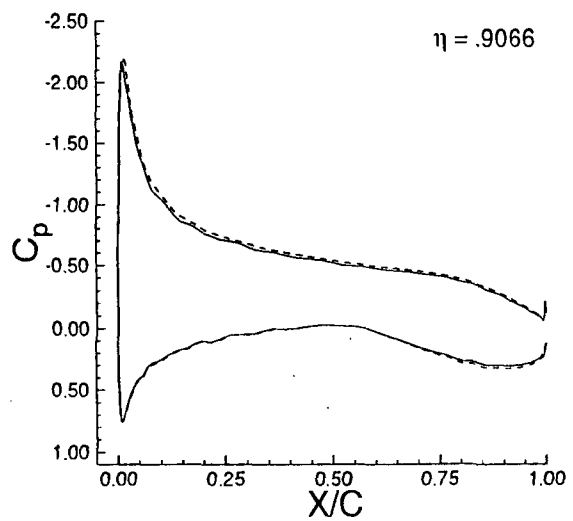

Figure 12: Comparison of computed full-span and semi-span pressure distributions ($M_\infty = .20$, $\alpha = 4.43°$, $Re = 4.2 \times 10^6$).

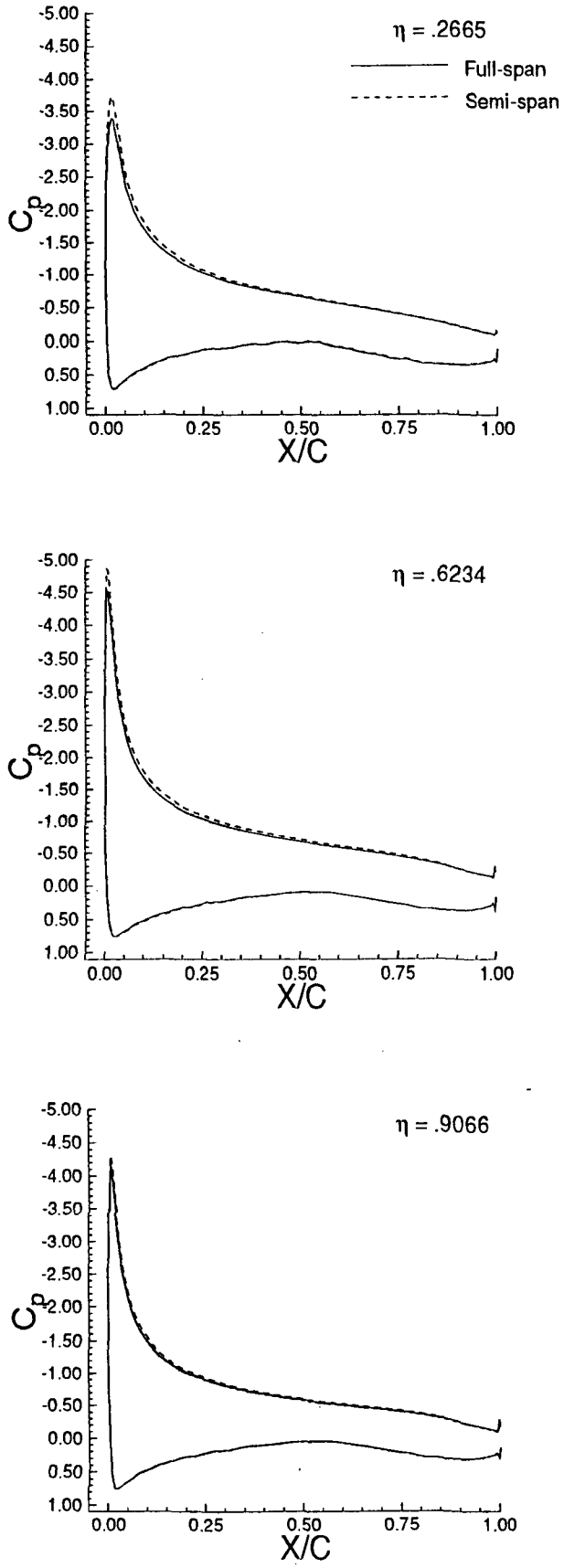

Figure 13: Comparison of computed full-span and semi-span pressure distributions ($M_\infty = .20$, $\alpha = 8.58°$, $Re = 4.2 \times 10^6$).

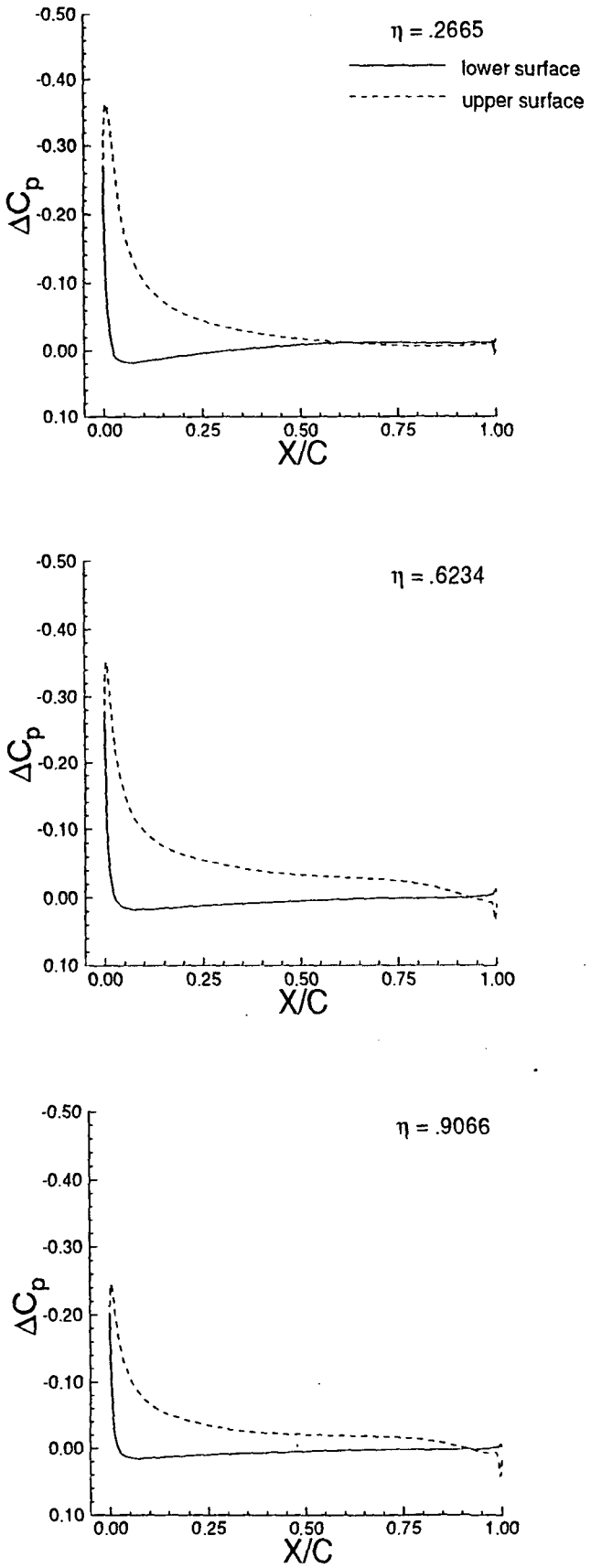

Figure 14: Computed differential pressure distributions ($M_\infty = .20$, $\alpha = 8.58°$, $Re = 4.2 \times 10^6$).

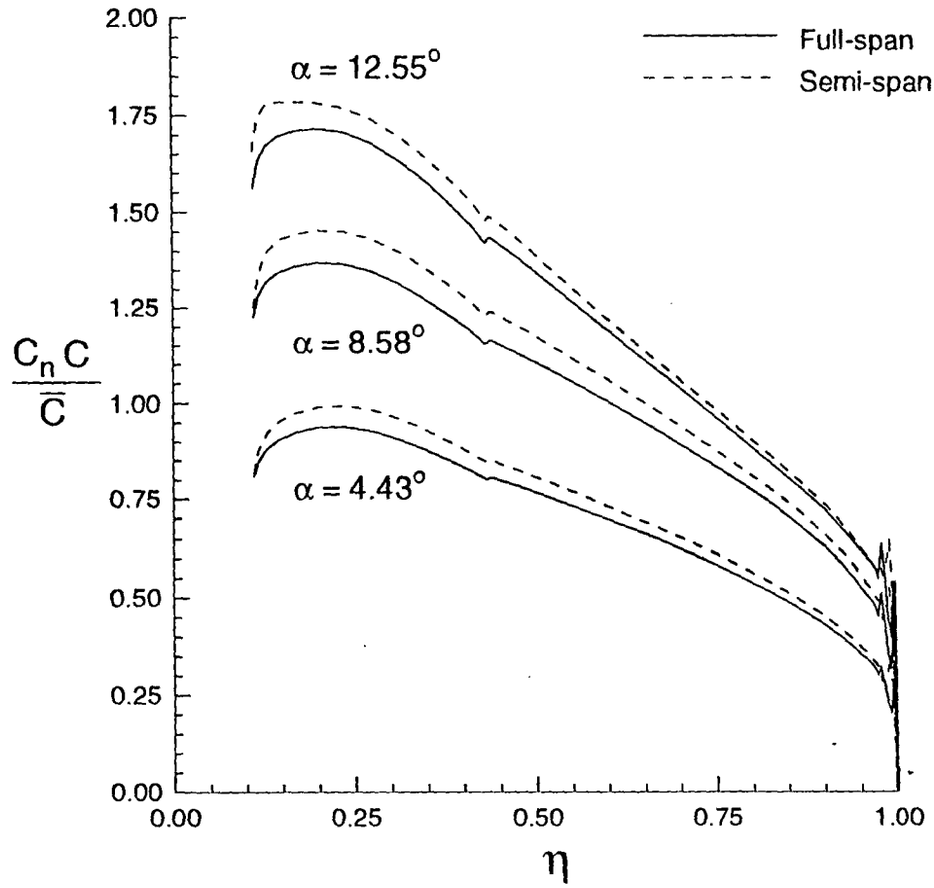

Figure 15: Comparison of computed spanload distributions (M_∞ = .20, Re = 4.2 x 10^6).

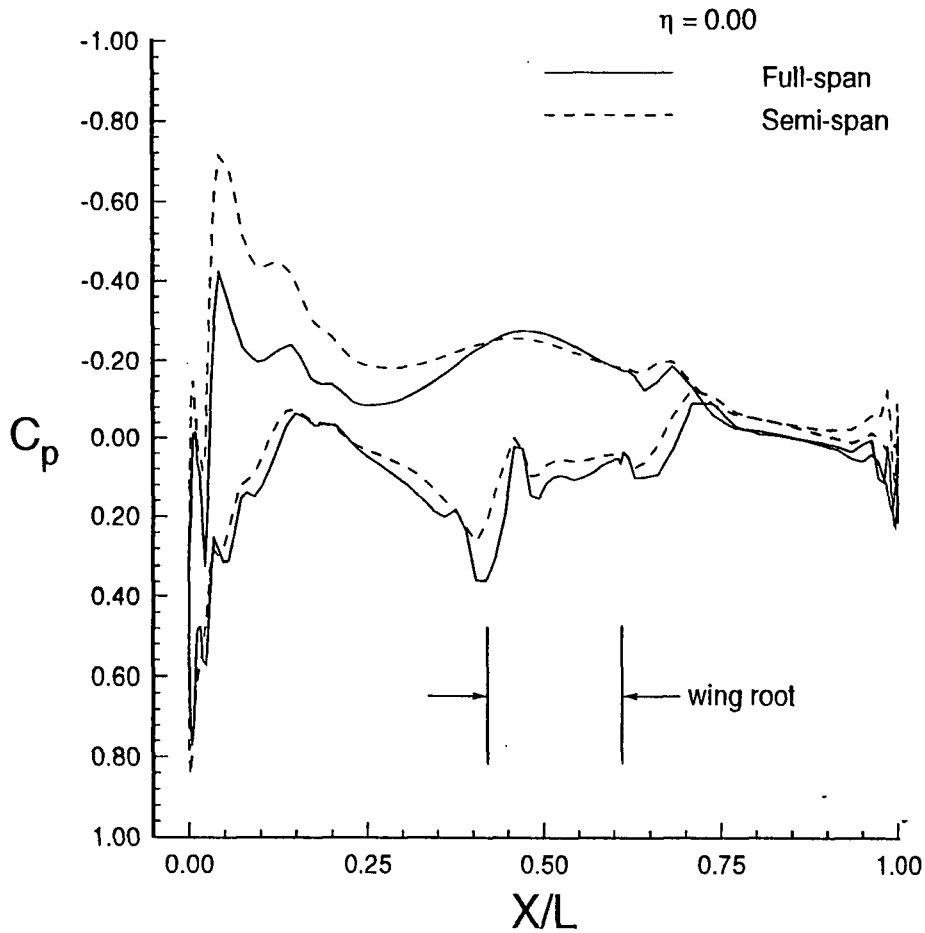

Figure 16: Comparison of computed full-span and semi-span fuselage centerline pressure distributions ($M_\infty = .20$, $\alpha = 12.55°$, $Re = 4.2 \times 10^6$).

Full-span

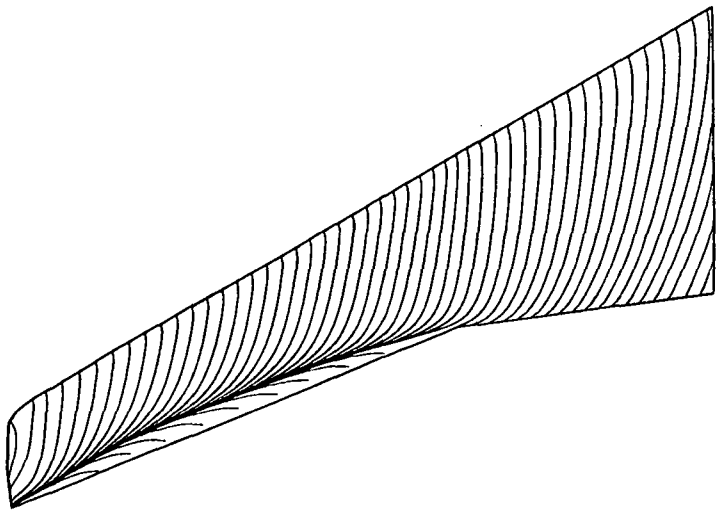

Semi-span

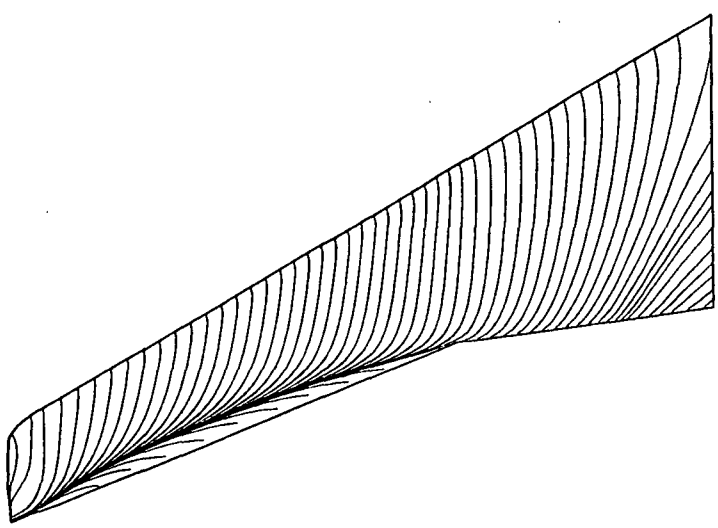

Figure 17: Comparison of computed full-span and semi-span upper wing surface streamline patterns ($M_\infty = .20$, $\alpha = 12.55°$, $Re = 4.2 \times 10^6$).

Full-span

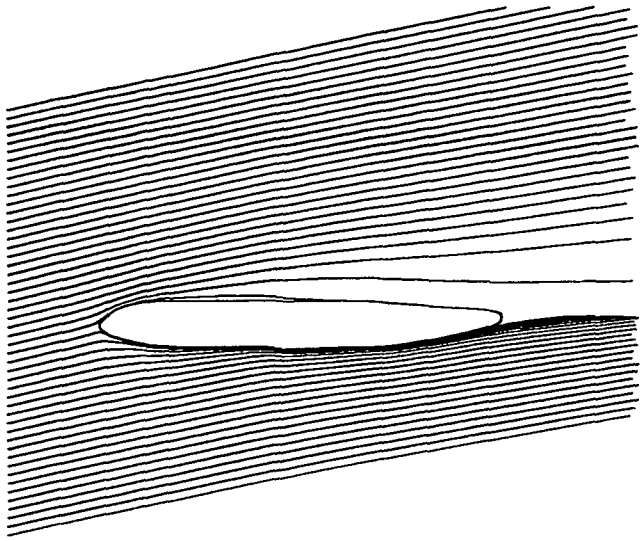

Semi-span

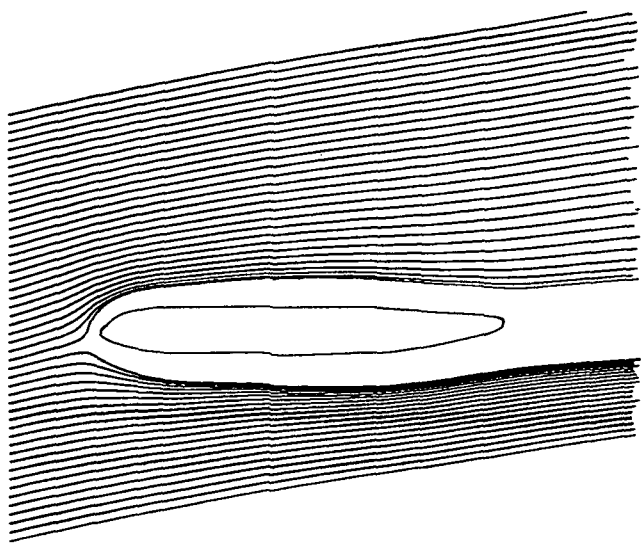

Figure 18: Comparison of computed full-span and semi-span root plane streamline patterns ($M_\infty = .20$, $\alpha = 12.55°$, $Re = 4.2 \times 10^6$).

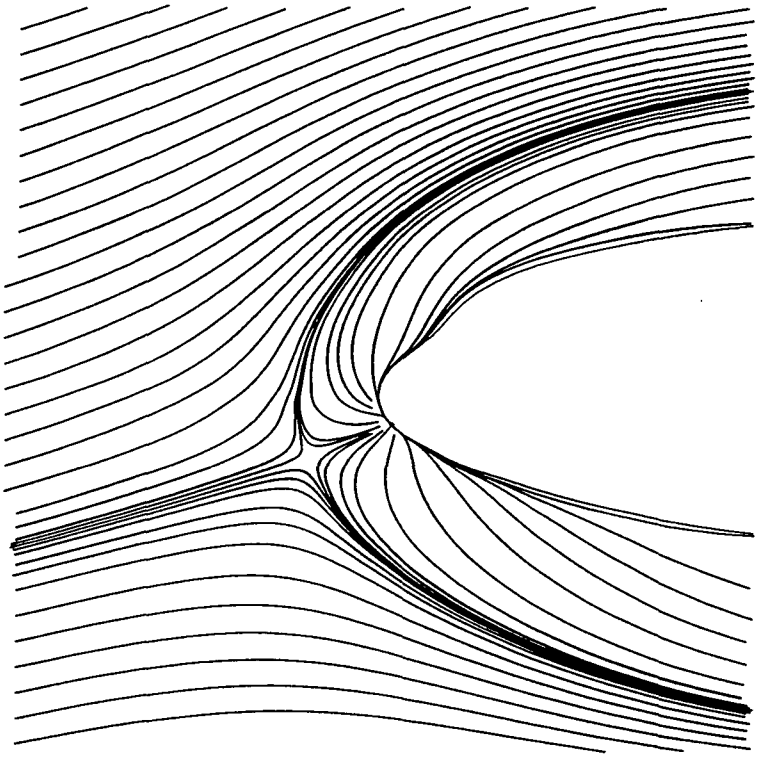

Figure 19: Computed sidewall streamline pattern in nose region ($M_\infty = .20$, $\alpha = 12.55°$, Re = 4.2 x 10^6).

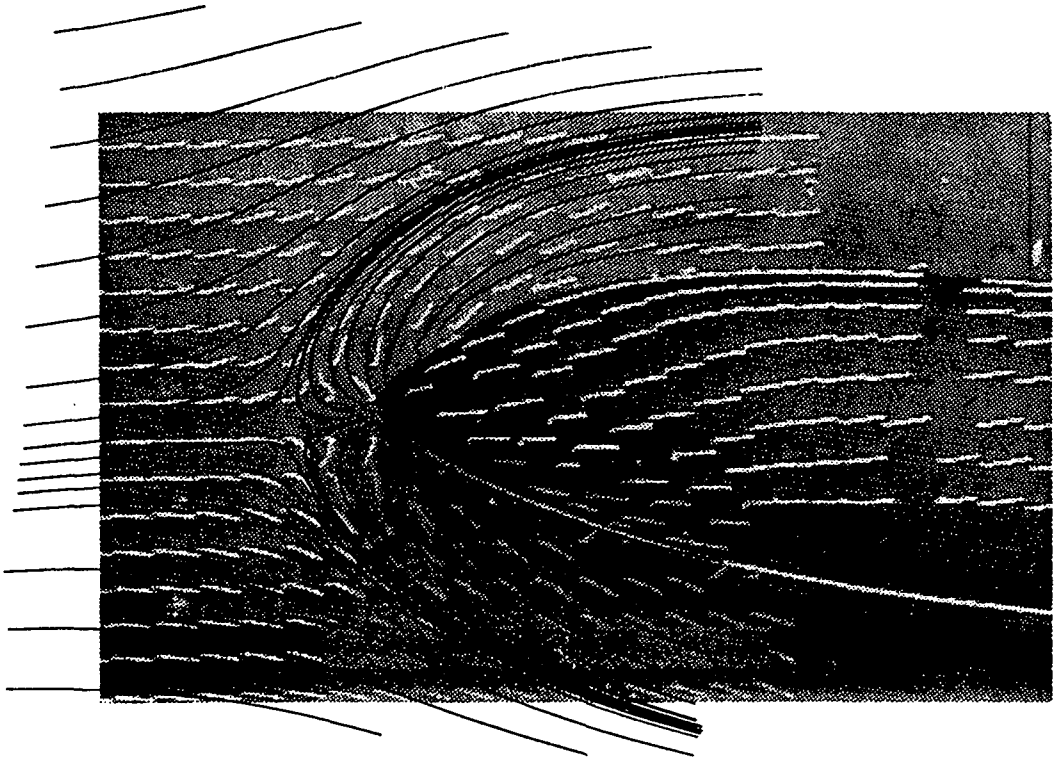

Figure 20: Comparison of computed sidewall streamline pattern and experimental tuft visualization results ($M_\infty = .20$, $\alpha = 8.24°$, Re = 4.2 x 10^6).